Small-Signal Analysis of Naturally-Sampled Single-Edge PWM Control Loops

Hendrik du Toit Mouton, *Member, IEEE*, Stephen Michael Cox, Brendan McGrath, *Senior Member, IEEE*, Lars Risbo, and Bruno Putzeys

(Highlighted Paper)

***Abstract*—This paper presents a simple method to analyze the behavior of feedback loops that contain a naturally-sampled single-edge pulse-width modulator. A small-signal model is derived by means of simple geometric arguments. It is shown how this small-signal model can be used to analyze the stability of the continuous-time pulse-width modulated feedback loop by using standard z-domain techniques. The strategy relies on familiar concepts like transfer functions and small-signal gains and does not require any in-depth knowledge of nonlinear systems. A simple design process, where the continuous-time compensator is designed directly in the z-domain, is developed and detailed design equations are derived for a PI current regulator. It is shown how the proposed strategy can accurately predict instability that cannot be explained by means of the well-known average model of the pulse-width modulator. The theoretical analysis is confirmed by means of detailed time-domain simulations. The mechanisms that lead to instability are discussed and an equation for the critical loop gain is derived.**

***Index Terms*—Bifurcation, pulse-width modulation, small-signal model, stability.**

I. Introduction

THE theory of the stability of pulse-width modulated control loops has been studied for more than half a century [1]–[6] and is almost as old as the field of Power Electronics itself. The most widely used method to derive a transfer function for a pulse-width modulated converter is the state-space averaging technique, introduced by Middlebrook and Cuk in [7]. The main advantages of state-space averaging are its simplicity and the fact that it can easily be applied to design problems by using techniques from classical linear control theory. One of the major disadvantages of this technique is the fact that it fails to predict the stability of even the simplest PWM feedback loops correctly [8].

Another technique that has gained popularity is generalized state-space averaging, which was introduced in [9]. According to this method, the circuit's state variables are approximated by a Fourier series of which the coefficients are time dependent. The greater the order of the harmonics considered in the model, the more accurate the model will become. This method was extended to include feedback in [10] and has since been the subject of intense research [11]–[14].

Over the years a vast number of different approaches have been developed to analyze the nonlinear behavior of power electronic converters. A complete summary of all these approaches would result in a substantial comprehensive survey paper and falls beyond the scope of the current paper. The following paragraphs provide an overview of the use of discrete-time small-signal models to analyze the behavior of continuous-time PWM control loops.

The first comprehensive study of the use of discrete-time models to analyze the small-signal behavior of power electronic converters can be found in [15]. The basis for this work is to utilize straight-line approximations to study the steady-state behavior of the converter. In [16], the full state-space equations that describe the nonlinear system are derived. The steady-state operating point is determined through simulation, after which the system is linearized to produce a small-signal model. The eigenvalues of the linearized model are used to analyze the stability of the converter. In [17], a linear small-signal model is derived which gives rise to a discrete-time modeling approach, based on the state-space representation of the converter. A general approach to sampled-data modeling of power electronic converters is described in [18]. This approach requires the use of symbolic computer manipulation to calculate the matrix exponentials that arise when modeling the system. It then makes use of multivariable Taylor series expansions to derive the small-signal model. The approach followed in [19] is broadly similar to that of [16]. The differential equations that describe the full nonlinear system are derived and the steady-state operating point is determined through simulation. Standard mathematical linearization techniques are then applied to derive a linear sampled-data model. A unified framework for modeling closed-loop PWM dc-to-dc converters based on concepts from Banach spaces and the time-lifting technique is presented in [20]. In [21], previously developed sampled-data modeling techniques

Manuscript received September 6, 2016; revised December 1, 2016; accepted January 4, 2017. Date of publication February 8, 2017; date of current version October 6, 2017. Recommended for publication by Associate Editor L. Corradini.

H. du T. Mouton is with the Department of Electrical and Electronic Engineering, University of Stellenbosch, Matieland 7602, South Africa (e-mail: dtmouton@sun.ac.za).

S. M. Cox is with the School of Mathematical Sciences, University of Nottingham, Nottingham NG7 2RD, U.K. (e-mail: stephen.cox@nottingham.ac.uk).

B. McGrath is with the School of Electrical and Computer Engineering, RMIT University, Melbourne, Vic. 3000, Australia (e-mail: brendan.mcgrath@rmit.edu.au).

L. Risbo and B. Putzeys are with the Purifi ApS, Højbjerg 8270, Denmark (e-mail: lars@purifi.dk; bruno.putzeys@gmail.com).

This paper has supplementary downloadable multimedia material available at http://ieeexplore.ieee.org provided by the authors. The material contains a PowerPoint presentation. This material is 1.33 MB in size.

Color versions of one or more of the figures in this paper are available online at http://ieeexplore.ieee.org.

Digital Object Identifier 10.1109/TPEL.2017.2666720

in [9], [15], and [17] are used to obtain a discrete-time model of a dual active-bridge converter.

The idea of using discrete-time models to analyze the behavior of continuous-time pulse-width modulated control loops developed independently in the class-D audio community. It is imperative to have accurate models when designing high-performance class-D amplifiers since very high loop gains are required to obtain a flat frequency response over the audio band, low output impedance, and sufficient noise and error suppression. In [22], a small-signal model that leads to a discrete-time model is derived within the context of generalized carriers with double-edge modulation. While the small-signal model of [22] is derived in a similar way to that of [17], the small-signal model of [22] incorporates the effect of the ripple gradient into the small-signal model itself. Applications of this model are described in [23] and [24]. It should be pointed out that the discrete-time analysis of the double-edge modulator in [22] is accurate only near a steady-state operating point with a 50% duty cycle idle point. In [25], a discrete-time model of a class-D amplifier that incorporates the ripple compensation technique of [26] was derived and used to analyze the steady-state response, the stability of the steady-state solution and to derive a small-signal model as well as a large-signal model of the loop.

This paper shows how the small-signal behavior of a continuous-time control loop, containing a naturally-sampled single-edge pulse-width modulator, can be studied by using well-known techniques from classical control theory. A small-signal model is derived, according to which the pulse-width modulator is modeled as an ideal sampler and an impulse generator. It is shown that the small-signal gain of the pulse-width modulator depends on the ripple gradient of the input signal to the pulse-width modulator. It is subsequently shown how the continuous-time feedback loop can be transformed to the z-domain, where standard z-domain methods can be used to analyze its stability. A major advantage of this approach is that it leads to a simple z-domain design strategy which yields the coefficients of the continuous-time controller. Detailed design equations are developed for a PI current regulator. An analytic equation for the small-signal gain, which previously had to be determined through time-domain simulations, is derived. The concept of the critical loop gain is introduced and a closed-form solution for the value of the critical loop gain is derived.

The strategy presented here does not require any specialized knowledge of nonlinear control systems. It is based on familiar concepts like transfer functions and loop gains and can easily be applied by practising engineers to design high-performance control loops. The methods discussed in this paper provide significant physical insight into the mechanisms that govern the stability of naturally-sampled control loops, thereby demystifying some of the behavior that cannot be explained by means of the average model.

The work discussed in this paper is not limited to analog control loops, but is also applicable to highly oversampled digital control loops, in which the sampling frequency is significantly higher than the switching frequency. The design and FPGA implementation of a highly oversampled digital current regulator is discussed in [27].

The small-signal model of the single-edge naturally-sampled pulse-width modulator is derived in Section II. In Section III, it is systematically explained why the small-signal model accurately predicts the stability of the large-signal nonlinear feedback loop. The use of z-domain methods to model the small-signal feedback loop is discussed in Section IV, while an analytic expression for the small-signal gain is derived in Section V. New design equations for a PI current regulator are presented in Section VI. The theoretical results of the previous sections are compared with time-domain simulations in Section VII, which also contains a detailed discussion of the mechanisms that lead to instability and an equation for the critical loop gain.

II. Small-Signal Model of the Single-Edge Pulse-Width Modulator

Numerous ways to analyze the small-signal behavior of power electronic converters have been developed over the past decades [8], [12], [13], [28]. The small-signal model described in this section is derived by means of simple and intuitive geometric arguments.

In Fig. 1(a), a large signal $f(t)$ is applied to the input $p_i(t)$ of the single-edge naturally-sampled pulse-width modulator. The pulse-width modulator compares $f(t)$ to a sawtooth carrier and generates a PWM pulse train denoted by $p(t)$. For the sake of simplicity, it is assumed that the amplitude of the carrier is equal to 1. It is also assumed that the pulse-width modulator contains set-reset logic and will thus only respond to the first intersection between its input signal $f(t)$ and the carrier during each switching period.

A small perturbation signal $\tilde{f}(t)$ is added to $f(t)$ in Fig. 1(b) and applied to the input of the pulse-width modulator. In comparison with Fig. 1(a), the falling pulse edges in Fig. 1(b) are slightly shifted in time due to this perturbation signal. The resulting PWM pulse train is denoted by $p(t) + \tilde{p}(t)$. The narrow rectangular pulses on the right-hand side of Fig. 1(c) show the difference between $p(t)$ and $p(t) + \tilde{p}(t)$. The height of each rectangular pulse is equal to 2 (i.e., the peak-to-peak amplitude of the PWM pulse train) and its width corresponds to the time shift in the falling pulse edges resulting from $\tilde{f}(t)$. The distance between successive pulses is approximately equal to the switching period T_s.

It is well known that a sequence of narrow rectangular pulses can be modeled by a sequence of impulses (Dirac delta distributions) [29], as shown in Fig. 1(c). The strength of each impulse is equal to the area of the narrow rectangular pulse it represents. The small-signal model of the pulse-width modulator is a mathematical model that will produce the sequence $\tilde{p}(t)$ of impulses at its output, if its input signal is $\tilde{f}(t)$.

Up to this point, the derivation of the small-signal model is almost identical to that of [17]. One major difference is the fact that the bus voltage of the converter is taken as the input signal in [17]. As a result, the strategy presented in [17] can be used to analyze the stability of the loop. However, it cannot be used to derive a closed-loop reference-to-output transfer function of the loop. It will later be shown in (8) that the approach that is followed in the current paper does lead to a closed-loop small-signal transfer function.

Fig. 2 shows a zoomed view of one of the narrow rectangular pulses. The sampling time t_{sp} is defined as the time instant at which the large signal $f(t)$ intersects the carrier. Given that the gradient of the carrier is equal to $\frac{2}{T_s}$, where $T_s = \frac{1}{f_s}$ is the switching period, then by simple geometrical arguments (or

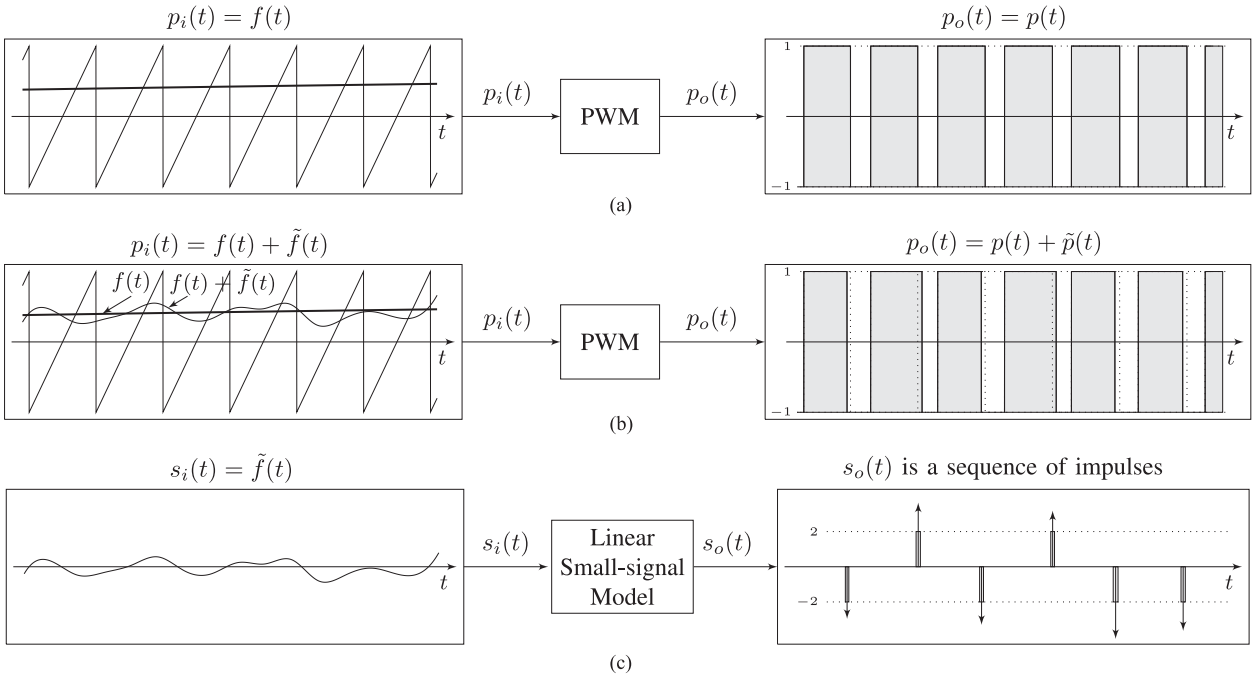

Fig. 1. Derivation of the small-signal model of the pulse-width modulator. (a) Reference signal $f(t)$ is applied to the input of the modulator. This produces a PWM pulse train denoted by $p(t)$. (b) Reference signal $f(t)$ plus a small perturbation signal $\tilde{f}(t)$ is applied to the input of the modulator. This produces a PWM pulse train denoted by $p(t) + \tilde{p}(t)$. (c) The sequence $\tilde{p}(t)$ of narrow rectangular pulses is the difference between the PWM pulse trains in (a) and (b). This sequence of narrow rectangular pulses is modeled as a sequence of impulses. The strength of each impulse is equal to the area of the narrow rectangular pulse it represents.

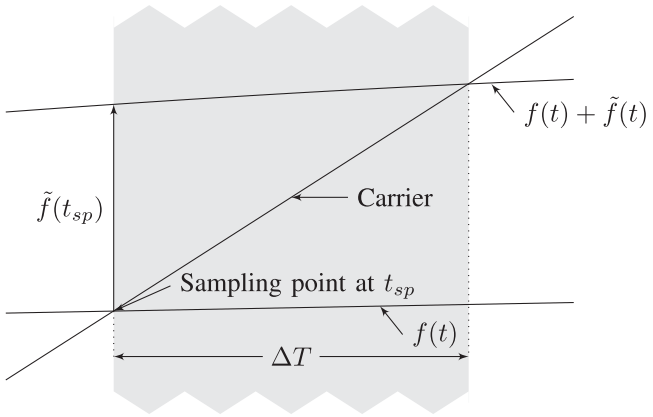

Fig. 2. Zoomed view of the perturbed and unperturbed intersection points, leading to a narrow rectangular pulse.

by Taylor-series expansion of the right-hand side of (1) and truncation at first order in small terms) it is straightforward to show that

$$\frac{2}{T_s}\Delta T = f(t_{\rm sp} + \Delta T) + \tilde{f}(t_{\rm sp} + \Delta T) - f(t_{\rm sp}) \quad (1)$$

$$\approx f'(t_{\rm sp})\Delta T + \tilde{f}(t_{\rm sp}) \quad (2)$$

where $f'(t_{\rm sp})$ is the derivative of the large-signal modulator input $f(t)$ at the sampling point.

Due to the fact that ΔT is small, two approximations were made to derive (2) from (1). The first approximation is that

$$\frac{f(t_{\rm sp} + \Delta T) - f(t_{\rm sp})}{\Delta T} \approx f'(t_{\rm sp}).$$

The second approximation is that $\tilde{f}(t_{\rm sp} + \Delta T) \approx \tilde{f}(t_{\rm sp})$.

Solving for ΔT from (2) yields

$$\Delta T \approx \frac{\tilde{f}(t_{\rm sp})}{2f_s - f'(t_{\rm sp})}.$$

Since the height of the rectangular pulse is equal to 2, the area A of the pulse is given by

$$A \approx \frac{2}{2f_s - f'(t_{\rm sp})}\tilde{f}(t_{\rm sp}). \quad (3)$$

It is thus evident that the area of each narrow rectangular pulse (and hence the strength of the impulse that represents it) is proportional to the value of the small-signal perturbation $\tilde{f}(t_{\rm sp})$, and depends on the derivative of the large-signal input $f'(t_{\rm sp})$ at the sampling point. Equation (3) can be rewritten as

$$A \approx \tilde{f}(t_{\rm sp})K_{\rm ss}T_s,$$

where

$$K_{\rm ss} = \frac{2f_s}{2f_s - f'(t_{\rm sp})}. \quad (4)$$

$K_{\rm ss}$ is called the small-signal gain of the pulse-width modulator. It depends on the switching frequency f_s as well as the gradient of the input signal to the pulse-width modulator just prior to its intersection with the carrier. This gradient will subsequently be referred to as the ripple gradient.

Fig. 3 shows the resulting equivalent block diagram of the PWM small-signal model. It consist of an ideal sampler, which samples its input signal at each intersection of the carrier and the input signal of the pulse-width modulator, i.e., the sampling point. The value of $\tilde{f}(t_{\rm sp})$ is multiplied by the small-signal gain

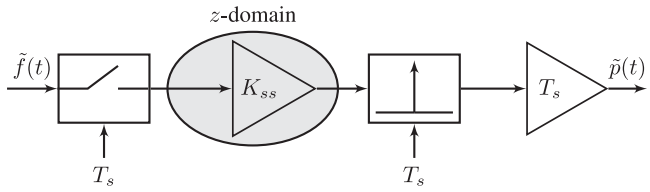

Fig. 3. Small-signal model of the single-edge pulse-width modulator.

$K_{\rm ss}$ and sent to an impulse generator which instantaneously produces an impulse of strength $\tilde{f}(t_{\rm sp})K_{\rm ss}$. This impulse is subsequently multiplied by a factor T_s. This happens once per switching period. The resulting sequence of numbers can be seen as a discrete-time signal which can be analyzed by using z-domain methods. This will be discussed in more detail in Section IV. The small-signal model of [17] does not incorporate the effect of the ripple gradient into the small-signal model itself. The effect of the ripple gradient has to be incorporated in the so-called effective gain vector in [17]. However, it is not explained how to do this for a carrier-based PWM strategy in [17]. The effect of the ripple gradient is quite subtle and can easily be overlooked.

It is important to note that the small-signal model is linear. Furthermore, if $f(t)$ is periodic, so that $f(t+T_s)=f(t)$ for all t, then $K_{\rm ss}$ is constant and the sampling becomes strictly periodic. As a result, the small-signal model is both linear and time invariant when $f(t)$ is periodic. This assumption of periodicity is used throughout this paper.

Note that $f(t)$ is periodic for systems with a constant reference $i^\star(t)$. In this case, $f(t)$ consists of a dc component and a periodic ripple component. In [22], a similar small-signal model was derived for a double-edge modulator in the context of a generalized carrier. The small-signal model of the single-edge modulator is linear and time invariant for all constant values of duty cycle. This is a major advantage of the single-edge modulator in comparison with the double-edge modulator.

The small-signal model described in this section can also be derived through a number of more precise, but less intuitive approaches, for instance by truncating the Taylor series of the PWM nonlinearity derived in [30] or by the methods proposed in [25].

Small-signal models of regularly-sampled pulse-width modulators were derived in [31]–[33]. These small-signal models are widely used to design digital control loops with a sampling frequency that is equal to either the switching frequency or twice the switching frequency. In this case, the small-signal gain is constant due to the fact that the ripple gradient is constant in a sampled system. The fact that the output signal is sampled, at fixed points within each switching period, by the analog-to-digital converter results in a further simplification. As a result of these two facts, the small-signal models of digital control loops for regularly-sampled PWM control loops are simpler than those of continuous-time naturally-sampled PWM loops.

III. Using the Small-Signal Model to Analyze Stability

Although, a clear definition could not be found in the literature, the term small-signal model is usually associated with a linearization of the underlying nonlinear system around a fixed operating point [34, p. 54]. The aim of this section is to show how the small-signal model that was derived in the previous section can be utilized to analyze the stability of a PWM feedback loop.

Fig. 4(a) shows a typical continuous-time feedback loop containing a single-edge naturally-sampled pulse-width modulator. The reference $i^\star(t)$ is an arbitrary signal and emf(t) represents a counter emf, for example as may be found in machine or grid-connected applications. In the case of a dc-to-dc converter, $i^\star(t)$ would be a constant, while $i^\star(t)$ would typically be a sinusoidal reference in the case of a dc-to-ac converter. With the exception of the pulse-width modulator, all components in the loop are assumed to be linear.

Since the pulse-width modulator is nonlinear, the system of differential equations that describe the loop is nonlinear. Due to the fact that the switching frequency is fixed, all the state-variables are periodic functions of time in the steady state. These state-variables form a closed phase path (also known as a trajectory or orbit) in state space, which is generally referred to as a limit cycle. In general, this limit cycle is not a fixed point in state-space, even when the reference $i^\star(t)$ is constant.

A perturbation analysis [35] is performed to analyze the input-output stability of this limit cycle. A small perturbation $\tilde{i}^\star(t)$ is superimposed on reference $i^\star(t)$ in Fig. 4(b). The question of the stability of the underlying limit cycle, is whether such a small perturbation to the reference causes corresponding small perturbations to the output signal $i(t)$ to grow over time or not. The input signal to the pulse-width modulator is now represented by $f(t)+\tilde{f}(t)$ and its output signal is $p(t)+\tilde{p}(t)$. The output signal of the control loop is $i(t)+\tilde{i}(t)$.

Fig. 4(c) shows an equivalent representation of Fig. 4(b). Since $\tilde{f}(t)$ is assumed to be a small perturbation signal, the pulse-width modulator of Fig. 4(b) can be replaced with a pulse-width modulator with input signal $f(t)$ and a PWM small-signal model with input signal $\tilde{f}(t)$.

Note that all the components in the lower branch of Fig. 4(c), i.e., the compensator, PWM small-signal model and plant are linear. As a result, it is easily shown by block diagram manipulation, that Fig. 4(d) is equivalent to Fig. 4(c). As a final step, the top branch of Fig. 4(d) can be replaced by Fig. 4(a), as shown in Fig. 4(e).

Fig. 4(e) shows how the perturbed nonlinear feedback loop of Fig. 4(b) has now been separated into two parts. The top branch represents the original feedback loop of Fig. 4(a), which operates in a limit cycle. This branch will be referred to as the large-signal loop. The bottom branch is the small-signal loop and is a linear feedback loop. The location of the sampling instants as well as the small-signal gain are determined by the large-signal loop. Note that the stability of the large-signal limit cycle is reduced to analyzing the stability of the linear small-signal feedback loop. It is important to note that the small-signal circuit is not a linearization around a fixed operating point, but rather a linearization around the large-signal limit cycle.

The small-signal model is linear and provides accurate information about the behavior of the system in the vicinity of the original limit cycle. It can subsequently be used to analyze its stability. In general, the small-signal model does not provide other information about the large-signal behavior of the system. Since the large-signal loop is nonlinear, it cannot itself be

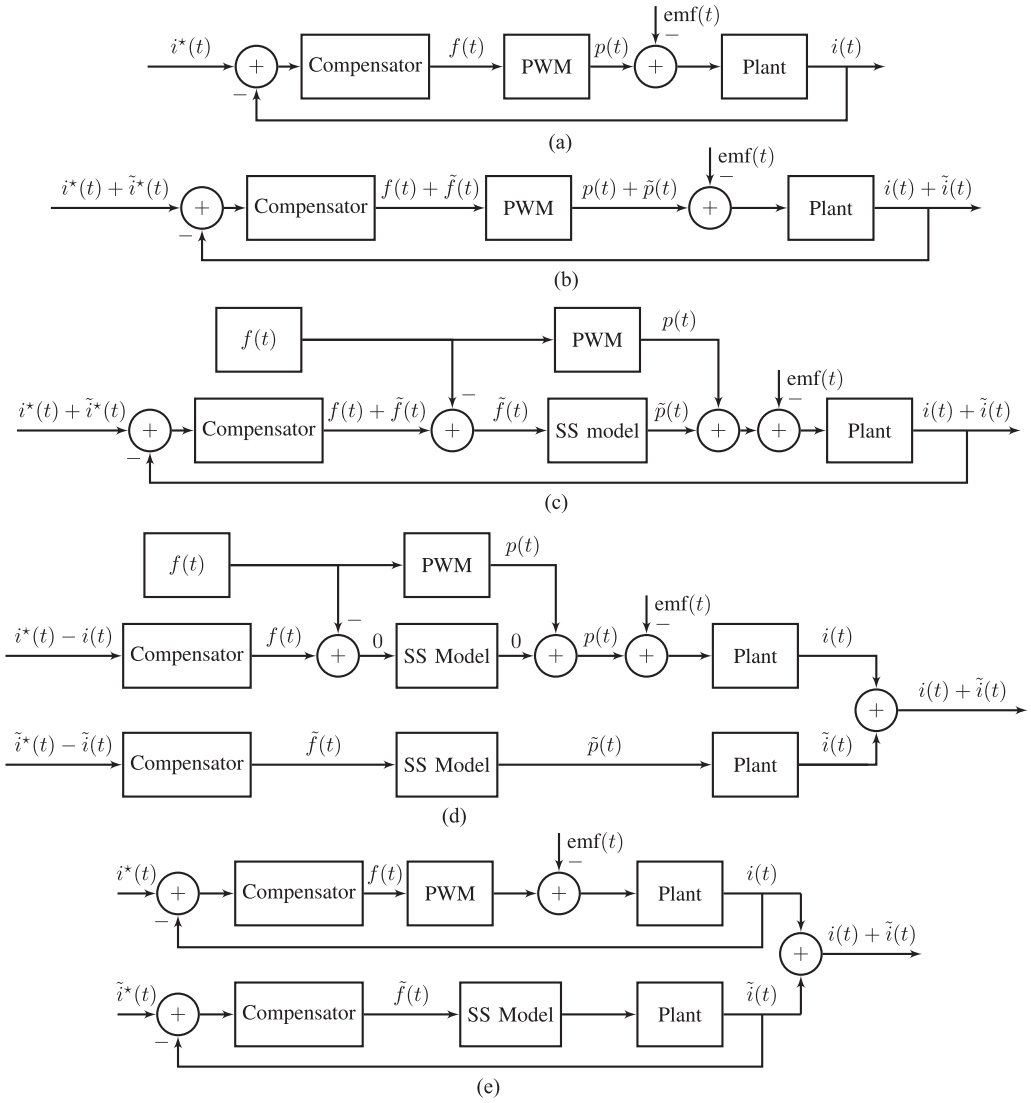

Fig. 4. Splitting the loop into separate large-signal and small-signal loops. (a) PWM feedback loop with reference $i^\star(t)$. (b) PWM feedback loop with perturbed reference $i^\star(t)+\tilde{i}^\star(t)$. (c) Equivalent representation of the block diagram in (b). (d) By linearity, the lower branch of (c) can be split into two separate branches. (e) The top branch of (d) is replaced by (a).

described by concepts from the theory of linear systems, like eigenvalues, and transfer functions.

IV. z-Domain Modeling of the Small-Signal Feedback Loop

Fig. 5 shows the small-signal model of Fig. 3 embedded in the lower branch of Fig 4(e). As mentioned previously, the signal passing from the ideal sampler to the impulse generator in Fig. 5 can be seen as a discrete-time signal that describes the small-signal evolution of the duty cycle perturbation. In this section, it is shown how this discrete-time signal can be studied by making use of standard z-domain methods.

In order to characterize the circuit from the perspective of this discrete-time domain, the link between the sampler and impulse generator in Fig. 5 is temporarily broken and the impulse generator emits a single impulse to characterize the surrounding linear circuit. The ideal sampler starts sampling at the same instant with its sampling frequency equal to the switching frequency.

Let $G(s)$ denote the open-loop s-domain transfer function of the surrounding continuous-time feedback loop, i.e., $G(s)=G_c(s)G_p(s)$, where $G_c(s)$ is the compensator transfer function and $G_p(s)$ the plant transfer function. By expanding $G(s)$ into partial fractions [29] it can be written in the form

$$G(s)=\sum_{k=1}^{K}\frac{A_k}{s+p_k} \tag{5}$$

where the poles $-p_1,-p_2,\ldots,-p_K$ are assumed to lie in the left-half of the complex plane. The z-domain transfer function $G_z(z)$ is obtained by sampling the impulse response $g(t)$ of $G(s)$, i.e.,

$$\begin{aligned} G_z(z) &= T_s\sum_{n=1}^{\infty} g(nT_s)z^{-n} \\ &= T_s\sum_{k=1}^{K} A_k\left(\sum_{n=1}^{\infty} e^{-np_kT_s}z^{-n}\right). \end{aligned} \tag{6}$$

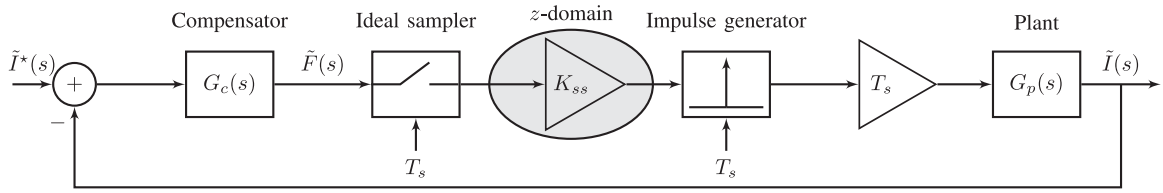

Fig. 5. PWM small-signal model embedded in the feedback loop.

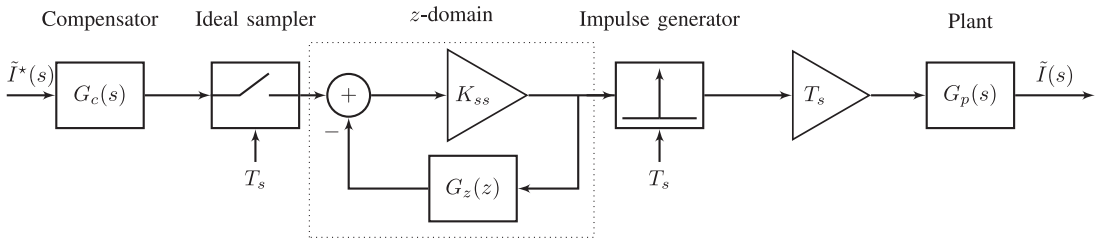

Fig. 6. Equivalent block-diagram representation of Fig. 5. Note that the only feedback loop is in the z-domain.

Note that each of the infinite sums in (6) forms a geometric series. By using the well-known equations [36] for the sum of a geometric series, each of the infinite sums in (6) can be rewritten as

$$\sum_{n=1}^{\infty} e^{-np_kT_s} z^{-n} = \frac{e^{-p_kTs}}{z - e^{-p_kT_s}}$$

provided that $|z| > \left|e^{-p_kT_s}\right|$. Hence

$$G_z(z) = T_s \sum_{k=1}^{K} A_k \frac{e^{-p_kTs}}{z - e^{-p_kT_s}}. \tag{7}$$

It is important to note that the first sample of the impulse response, corresponding to $n = 0$, was ignored. This is because practical systems will always contain a nonzero propagation delay [17], [22]. As a result, the first sample would always be zero.

This method of transforming from the s-domain to the z-domain is a modified version of the well-known impulse-invariance method. This transformation maps the s-domain pole $-p_k$ onto the z-domain pole $e^{-p_kT_s}$. There is no simple way of mapping the s-domain zeros onto the z-domain zeros. The locations of the z-domain zeros depend on the location of the poles and their weights in the partial fraction expansion of (5). It should be noted that only s-domain poles in the left-half of the complex plane were considered. The theory can also be extended to poles on the imaginary axis as well as higher order poles. For the sake of simplicity it will be assumed that poles on the imaginary axis are located slightly to the left of this axis. By making a slight modification to (7), it is possible to include the effect of transport delays as was shown in [27].

Fig. 6 can be derived from Fig. 5 through simple block-diagram manipulation. Since the only feedback loop in Fig. 6 is in the z-domain, the stability of the small-signal loop depends only on the stability of this z-domain loop.

It is well-known that the impulse generator in Fig. 6 generates images around integer multiples of the switching frequency in the frequency domain. Closer investigation of Fig. 6 yields a single-frequency small-signal closed-loop transfer function

$$\frac{\tilde{I}(\omega)}{\tilde{I}^{\star}(\omega)} = G_c(j\omega)\left[\frac{K_{\rm ss}}{1 + K_{\rm ss}G_z(e^{j\omega T_s})}\right] T_s G_p(j\omega). \tag{8}$$

This transfer function takes into account only the harmonic at one particular frequency. It does not account for the images generated by the impulse generator or the PWM sidebands generated by the pulse-width modulator. It is similar to the transfer characteristic measured by a narrow-band gain-phase analyzer. A similar transfer function was derived in [23] and [24] within the context of a generalized carrier.

V. Analytic Equation for the Small-Signal Gain

The PWM pulse train contains high-frequency ripple components that are injected back into the feedback loop. Fig. 7 shows a typical modulator input signal $f(t)$ as well as its output signal $p(t)$ in the steady state. The duty cycle is denoted by d. According to (4), the small-signal gain $K_{\rm ss}$ of the pulse-width modulator depends on the gradient of the input signal to the pulse-width modulator just prior to its intersection with the carrier. The small-signal gain would be equal to 1 in the absence of ripple feedback. In most cases, ripple feedback causes a reduction in the small-signal gain.

One solution to the problem of ripple feedback would be to place a low-pass filter in the feedback path to reduce the PWM ripple before entering the pulse-width modulator. However, the additional delay caused by this filter imposes unnecessary restrictions in terms of gain and bandwidth on the design of the regulator. Developing a clear understanding of the effect of ripple feedback makes it possible to design high-performance feedback loops without any unnecessary low-pass filtering.

To this end, a closed-form solution for the steady-state value of the ripple gradient was derived. The mathematical details of this derivation can be found in the appendix. The gradient $f'(t_{\rm sp})$ of the modulator input signal $f(t)$ just prior to its intersection

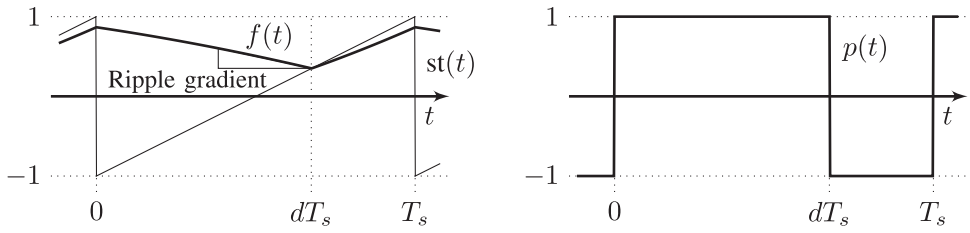

Fig. 7. Typical modulator input and output signals in the steady state.

TABLE I
SYSTEM PARAMETERS

Parameter	Symbol	Value
Inductor	L	17 mH
Resistor	R	10 Ω
Bus voltage	V_d	200 V
Switching frequency	f_s	5 kHz
Counter EMF	emf	30 V

with the carrier is given by

$$f'(t_{\rm sp}) = \lim_{\substack{t\to dT_s \\ t\le dT_s}} \left[\frac{df(t)}{dt}\right] = 2\sum_{k=1}^{K} A_k \left(\frac{e^{-p_k T_s} - e^{-p_k dT_s}}{1-e^{-p_k T_s}}\right). \tag{9}$$

According to (4), the small-signal gain $K_{\rm ss}$ of the pulse-width modulator is given by

$$K_{\rm ss} = \frac{f_s}{f_s - \sum_{k=1}^{K} A_k \left(\frac{e^{-p_k T_s} - e^{-p_k dT_s}}{1-e^{-p_k T_s}}\right)}. \tag{10}$$

As expected, the small-signal gain depends on the duty cycle of the pulse-width modulator and is equal to 1 when the duty cycle equals 1.

Remark: During the derivation of (9), it was assumed that all the poles of $G(s)$ are located in the left half of the complex plane. If p_k is located at the origin, i.e., $p_k = 0$, then the contribution of p_k to the sum in (9) can be calculated by taking the limit as $p_k \to 0$, i.e.,

$$\lim_{p_k\to 0} A_k \left(\frac{e^{-p_k T_s} - e^{-p_k dT_s}}{1-e^{-p_k T_s}}\right) = A_k(d-1).$$

VI. z-DOMAIN DESIGN STRATEGY

A major advantage of the small-signal model and the resulting z-domain analysis is that it gives rise to an accurate but simple design strategy. As an example, the design of a PI current regulator with an RL load as shown in Fig. 8 is outlined in this section. The gain block $K_{\rm ad}$ in Fig. 8 represents an additional gain term which will be used in subsequent sections. It is assumed that $K_{\rm ad} = 1$ throughout this section. The system parameters are shown in Table I.

Assume for the moment that the small-signal gain $K_{\rm ss}$ is equal to 1 and let $\tau := \frac{L}{R}$ denote the time-constant of the RL load. The open-loop transfer function $G(s)$ for the system of Fig. 8 is given by

$$G(s) = G_c(s)G_p(s) = \left(K_p + \frac{K_i}{s}\right)\left(\frac{\frac{V_d}{L}}{s+\frac{1}{\tau}}\right).$$

The first step is to expand $G(s)$ into partial fractions according to (5), i.e.,

$$G(s) = \frac{A_1}{s+p_1} + \frac{A_2}{s+p_2}$$

where

$$p_1 = 0, \quad p_2 = \frac{1}{\tau}, \quad A_1 = \frac{K_i V_d}{R} \text{ and } A_2 = V_d\left(\frac{K_p}{L} - \frac{K_i}{R}\right). \tag{11}$$

The next step is to transform the s-domain transfer function $G(s)$ to the z-domain by making use of the impulse-invariance method described by (7), i.e.,

$$\begin{aligned} G_z(z) &= V_d\left[\frac{K_i}{R}\frac{1}{z-1} + \left(\frac{K_p}{L} - \frac{K_i}{R}\right)\frac{e^{-\frac{T_s}{\tau}}}{z-e^{-\frac{T_s}{\tau}}}\right]T_s \\ &= \left[\frac{\frac{V_d T_s}{L}}{z-e^{-\frac{T_s}{\tau}}}\right]\left[K_p e^{-\frac{T_s}{\tau}} + \frac{K_i\tau\left(1-e^{-\frac{T_s}{\tau}}\right)z}{z-1}\right]. \end{aligned} \tag{12}$$

The first term of $G_z(z)$ represents the RL load. The s-domain pole located at $-\frac{1}{\tau}$ is mapped onto the z-domain pole at $e^{-\frac{T_s}{\tau}}$. It is quite interesting that the second term corresponds to the transfer function of a discrete-time PI controller [33] whose transfer function is of the form

$$G_{\rm PI}(z) = K_p' + K_i'\left(\frac{z}{z-1}\right) = K_p' + \frac{K_i'}{1-z^{-1}} \tag{13}$$

where

$$K_p' = K_p e^{-\frac{T_s}{\tau}} \quad \text{and} \quad K_i' = K_i\tau\left(1-e^{-\frac{T_s}{\tau}}\right). \tag{14}$$

Note that the two coefficients, K_p' and K_i', of the discrete-time PI controller are just scaled versions of the coefficients K_p and K_i of the original continuous-time PI controller $G_c(s)$.

A variety of design techniques can be utilized to design this discrete-time PI controller in the z-domain. Once the values of K_p' and K_i' are determined, the values of K_p and K_i can then be calculated from (14), yielding the continuous-time controller.

For this example it was decided to design for a crossover frequency ω_c of $2\pi \times 1000$ rad/s and a phase margin PM of 45° in the z-domain. It is well known that the frequency response of the z-domain transfer function $G_z(z)$ is obtained by evaluating $G_z(z)$ on the unit circle by setting $z = e^{j\omega T_s}$ [37]. By definition,

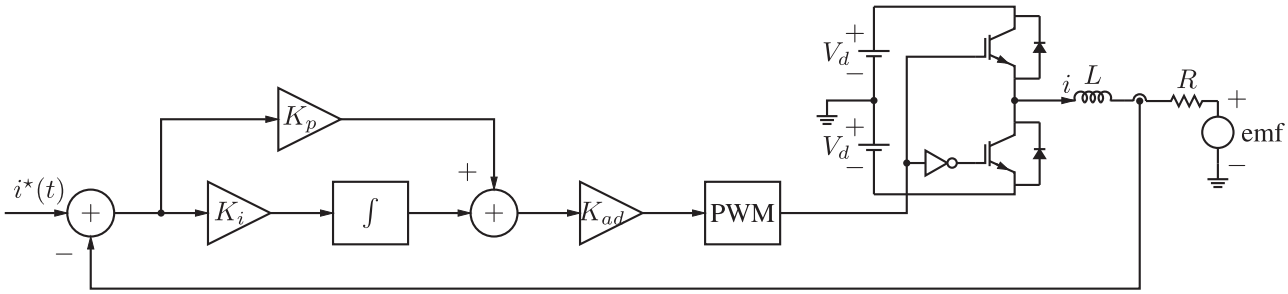

Fig. 8. Circuit used for the design example.

the magnitude of open-loop transfer function $G_z(e^{j\omega T_s})$ must be equal to 1 and its phase must be equal to $-(180^\circ - \text{PM})$ at the crossover frequency $\omega = \omega_c$, i.e.,

$$G_z(e^{j\omega_c T_s}) = e^{j\frac{(PM-180)\pi}{180}}.$$

According to (12) and (13), this implies that

$$e^{j\frac{(\text{PM}-180)\pi}{180}} = T_s \frac{V_d}{L\left(e^{j\omega_c T_s} - e^{-\frac{T_s}{\tau}}\right)}\left(K_p' + \frac{K_i'}{1-e^{-j\omega_c T_s}}\right).$$

Hence,

$$\frac{L}{T_s V_d}(e^{j\omega_c T_s} - e^{-\frac{T_s}{\tau}})e^{j\frac{(\text{PM}-180)\pi}{180}} = \left(K_p' + \frac{K_i'}{1-e^{-j\omega_c T_s}}\right).$$

By comparing the real and imaginary parts of the two sides of this equation, the following two expressions for K_i' and K_p' are derived:

$$K_i' = \frac{\Im(\gamma_1)}{\Im(\gamma_2)} \quad \text{and} \quad K_p' = \Re(\gamma_1 - K_i'\gamma_2) \qquad (15)$$

where γ_1 and γ_2 are defined as

$$\gamma_1 = \frac{L}{T_s V_d}(e^{j\omega_c T_s} - e^{-\frac{T_s}{\tau}})e^{j\frac{(\text{PM}-180^\circ)\pi}{180^\circ}}$$

and

$$\gamma_2 = \frac{1}{1-e^{-j\omega_c T_s}}.$$

Note that $\Re$ and $\Im$ denote the real and imaginary parts of a complex number, respectively.

Calculating the values of K_i' and K_p' from (15) yielded $K_i' = 0.1620$ rad/s and $K_p' = 0.3791$. The parameters K_p and K_i of the continuous-time PI controller were subsequently calculated from (14), which yielded $K_p = 0.4264$ and $K_i = 858.7758$ rad/s.

The next step is to take the dependence of the small-signal gain K_{ss} on the duty cycle d into consideration. Substituting the coefficients of (11) into (10), results in the following expression for the small-signal gain

$$K_{\text{ss}} = \frac{f_s}{f_s - V_d\left[\frac{K_i}{R}(d-1) + \left(\frac{K_p}{L} - \frac{K_i}{R}\right)\left(\frac{e^{-\frac{T_s}{\tau}} - e^{-\frac{dT_s}{\tau}}}{1-e^{-\frac{T_s}{\tau}}}\right)\right]}.$$

This equation was used to plot Fig. 9, which shows the small-signal gain as a function of the duty cycle. The small-signal gain varies between 0.5 and 1, with K_{ss} reaching 1 at a duty cycle of 1. This shows that the overall loop gain is reduced as a result of ripple feedback. Fig. 10 shows the open-loop Bode plot of $G_z(z)$ for the cases $K_{\text{ss}} = 1$ and $K_{\text{ss}} = 0.5$. The value of the phase-margin increases from 45° to 54° when the small-signal gain decreases from 1 to 0.5. At the same time the gain margin increases from 4.8 to 10.8 dB. This shows that the relative stability of the loop improves as K_{ss} is reduced. This justifies the assumption, made at the beginning of this

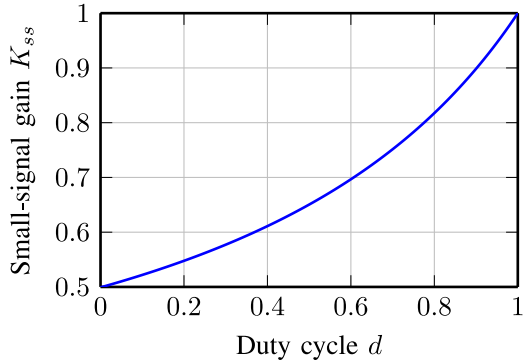

Fig. 9. Small-signal gain as a function of duty cycle.

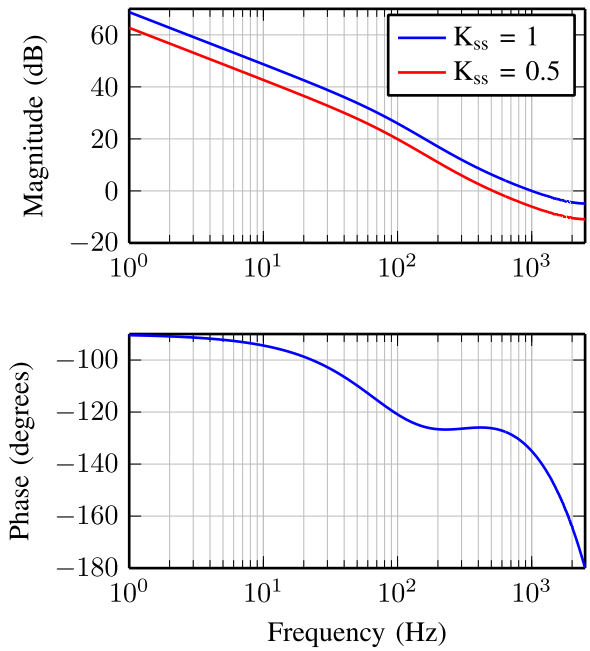

Fig. 10. Open-loop z-domain Bode plot.

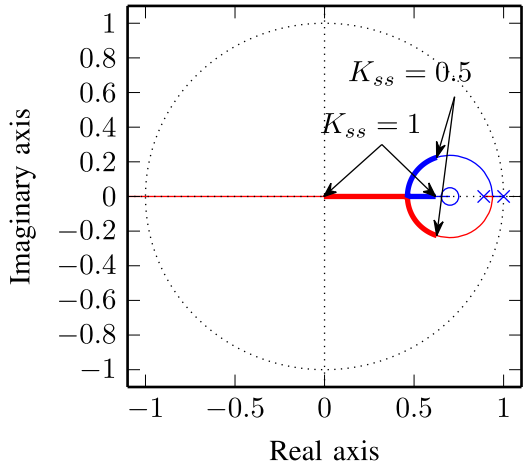

Fig. 11. z-domain root locus.

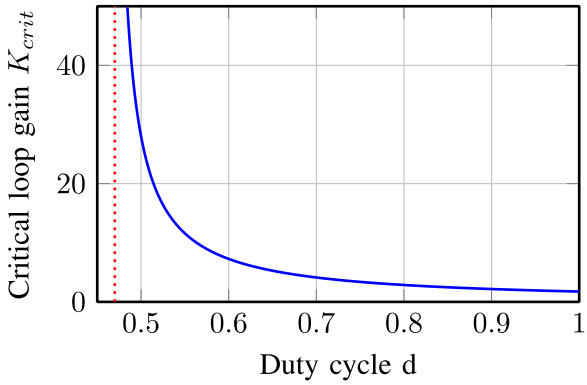

Fig. 12. Critical gain K_{crit} as a function of duty cycle. The asymptote is located at $d = 0.47$.

section, that $K_{\text{ss}} = 1$, since it results in a worst-case design. One disadvantage of the dependence of K_{ss} on the duty cycle is that fact that the crossover frequency is reduced from 1000 Hz when $K_{\text{ss}} = 1$ to 500 Hz when $K_{\text{ss}} = 0.5$. This has the effect that the small-signal bandwidth of the loop is reduced when the duty cycle is small. A ripple compensation strategy, which greatly reduces the dependence of the ripple gradient on the value of the duty cycle, is described in [27], [38], and [39].

Since the small-signal gain K_{ss} depends on the duty cycle, the locations of the closed-loop poles become dependent on the duty cycle as shown in the z-domain root locus of Fig. 11.

For more complex designs, a number of MATLAB functions and tools can be utilized during the design procedure. The residue function can be used to calculate the partial fraction expansion, while the Control System Designer can be used for the z-domain design.

A less precise design strategy was used to design a PR controller in [27], where the z-domain design was carried out by placing the open-loop zeroes and adjusting the gain by hand. Furthermore, the design process was not discussed in detail in [27] and the ripple gradient (and hence the small-signal gain) had to be determined by means of time-domain simulations. In [39], a state-of-the-art class-D amplifier with a fifth-order voltage control loop was designed by making use of a more sophisticated numerical design optimisation strategy. An experimental evaluation of this amplifier can be found in [39] and [40].

VII. Model Verification

This section presents a number of time-domain simulations of the controller designed in the previous section, to verify the validity of the small-signal model and the resulting z-domain analysis. In the process, the mechanisms that lead to instability are clarified, the concept of the critical loop gain is introduced and its closed-form mathematical expression is derived.

A. Gain Margin

In order to verify the gain margin predicted by the small-signal model, the value of the additional gain term K_{ad} in Fig. 8 is slowly ramped up and a bifurcation diagram is constructed to identify the value of K_{ad} at which instability occurs. When ramping up the value of K_{ad} the ripple gradient increases accordingly, thereby reducing the small-signal gain. The value K_{crit} of K_{ad} at which instability occurs is given by $G_m = K_{\text{ad}} K_{\text{ss}}$, where G_m is the gain margin of $G_z(z)$. According to (10), this occurs when

$$G_m = \frac{K_{\text{ad}} f_s}{f_s - K_{\text{ad}} \sum_{k=1}^{K} A_k \left(\frac{e^{-p_k T_s} - e^{-p_k dT_s}}{1 - e^{-p_k T_s}} \right)}.$$

Note that the term K_{ad} in the denominator accounts for the fact that the ripple gradient also increases by a factor K_{ad}. Solving for K_{crit} yields

$$K_{\text{crit}} = \frac{G_m f_s}{f_s + G_m \sum_{k=1}^{K} A_k \left(\frac{e^{-p_k T_s} - e^{-p_k dT_s}}{1 - e^{-p_k T_s}} \right)}.$$

Fig. 12 shows a graph of K_{crit} as a function of the duty cycle. For values of $d < 0.46$, it is impossible to make the loop go unstable by simply increasing K_{ad}. Increasing K_{ad} increases the ripple gradient. This results in a decrease in the small-signal gain K_{ss} which decreases more rapidly than K_{ad} increases, resulting in an overall decrease in gain in the region $d < 0.46$.

At a duty cycle of $d = 1$, the critical loop gain equals the gain margin of $G_z(z)$. This is due to the fact that the small-signal gain K_{ss} equals 1 when $d = 1$.

The value of K_{ad} was gradually ramped up over a period of 2000 s to generate the bifurcation diagrams of Fig. 13, in which the x-axis represents the value of K_{ad}. Such bifurcation diagrams are a valuable tool to analyze the stability of the underlying limit cycle. Since K_{ad} was ramped up linearly in time, the x-axis is a scaled version of the time axis. Each dot on the bifurcation diagram represents a value of the duty cycle. The duty cycle remains constant up to the bifurcation point, after which it starts to oscillate, indicating the onset of instability.

The dotted lines in these graphs indicate the critical value K_{crit} of K_{ad} according to the theory. The current reference in Fig. 13(a) was set to -10 A, which results in a duty cycle of 0.335. This value is less than 0.47 and hence, according to Fig. 12, the loop cannot be driven into unstable operation by increasing the value of K_{ad}. The simulated and theoretical bifurcation points in the other three graphs of Fig. 13 agree very well. In each case, the duty cycle starts to oscillate at half the switching frequency when the loop gain reaches the theoretical

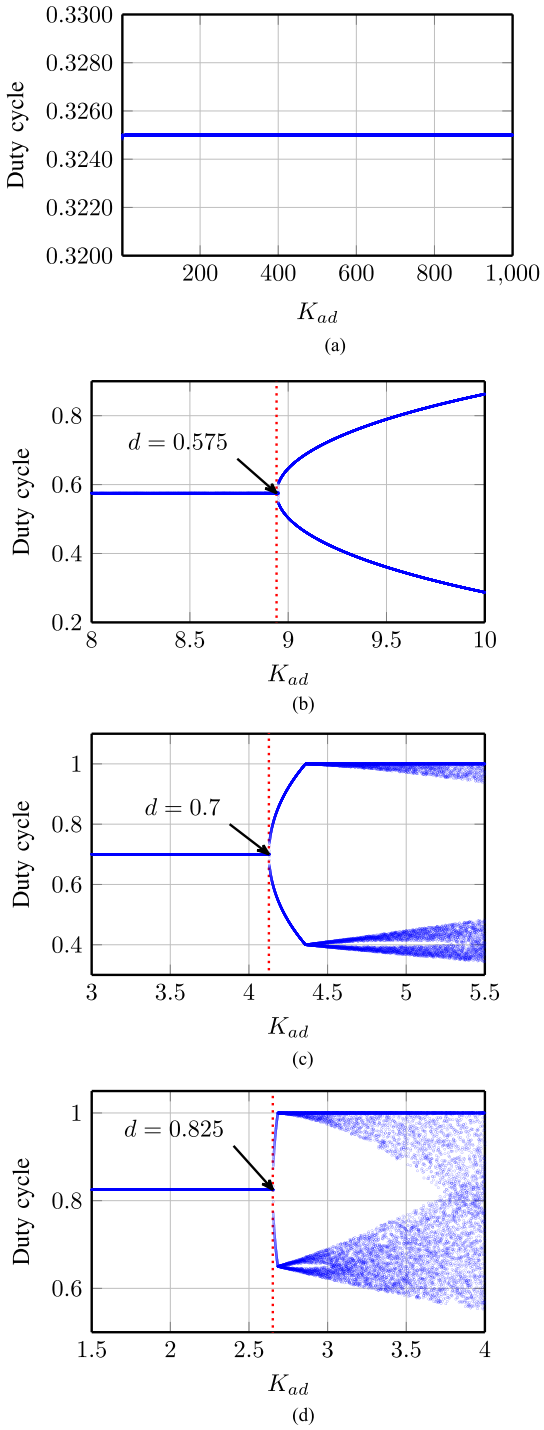

Fig. 13. Bifurcation diagrams. The dotted lines show the theoretical value of the critical loop gain. (a) Bifurcation diagram with $I_{\text{ref}} = -10$ A. (b) Bifurcation diagram with $I_{\text{ref}} = 0$ A. (c) Bifurcation diagram with $I_{\text{ref}} = 5$ A. (d) Bifurcation diagram with $I_{\text{ref}} = 10$ A.

stability boundary. The bifurcation is thus a period-doubling bifurcation, consistent with the fact that the z-domain root locus exits the unit circle at -1 in Fig. 11.

In a linear system, instability implies that at least one of the state variables will go to $\pm\infty$. In contrast, after the onset of instability at the bifurcation point in this nonlinear system, the loop simply changes its mode of operation, indicating that the bifurcation is *supercritical*. Another bifurcation occurs when K_{ad} is increased to the point where the pulse-width modulator is driven into saturation. The small-signal model presented in this paper only predicts the first bifurcation point. However, as can be seen for the bifurcation diagram with $I_{\text{ref}} = 10$ A, the second bifurcation can occur soon after the first bifurcation, when the converter operates at a duty cycle close to 1. As a result, the period-doubling mode of operation is seen as an unwanted mode.

It is important to point out that the traditional average model of the pulse-width modulator predicts an infinite gain margin, irrespective of the value of the duty cycle. It is thus evident that the average model does not provide an accurate indication of the stability margins of this simple control loop. This instability can be attributed to the sampling behavior of the pulse-width modulator.

B. Small-Signal Transient Response

Another way to validate the small-signal model is by simulating the transient response of the current regulator. A simulation of the converter was carried out in which the current reference $i^\star(t)$ was initially set to 0 A. The current reference was then ramped up from 0 to 1 A over a period of 2 ms as shown in Fig. 14(a). The z-domain feedback loop of Fig. 6 was also simulated to obtain the small-signal transient response. The results of this simulation are shown in Fig. 14(b), while Fig. 14(c) shows the duty cycle error [difference between the two curves in (b)]. The transient response predicted by the small-signal model corresponds closely to that of the simulation, with the maximum difference between the two being equal to approximately $5.3 \times 10^{-4} = 0.053\%$. Perfect agreement should not be expected since the small-signal model is a linearization of the nonlinear system.

C. Small-Signal Closed-Loop Transfer Function

The small-signal closed-loop transfer function predicted by (8) is verified in this section. In order to measure this transfer function through simulation, a sinusoidal signal $i^\star(t) = I\sin(\omega t)$ is used as the current reference for the circuit of Fig. 8 and the feedback loop is simulated in the time domain. The results from the first 20 ms of the simulation are discarded since they contain the start-up transient response of the loop. The remaining time-domain results are used to calculate the magnitude and phase of the harmonic at frequency ω of the output current $i(t)$. The magnitude of this harmonic is divided by the magnitude I of the reference $i^\star(t)$. This produces a dot on the magnitude plot of Fig. 15. The phase of the harmonic at ω of the output current i produces a dot at ω on the phase plot. The value of ω is increased and the process is repeated.

It is important to keep in mind that the impedance of the RL load increases with increasing frequency. Hence, the amplitude I of the reference $i^\star(t)$ must be decreased accordingly. The results of Fig. 15 were obtained with a maximum duty cycle deviation of 10%.

Fig. 15 also shows the magnitude and phase response of the small-signal transfer function according to (8) as well as the transfer function predicted by the average model of the pulse-width modulator. It is evident that, with the exception of the

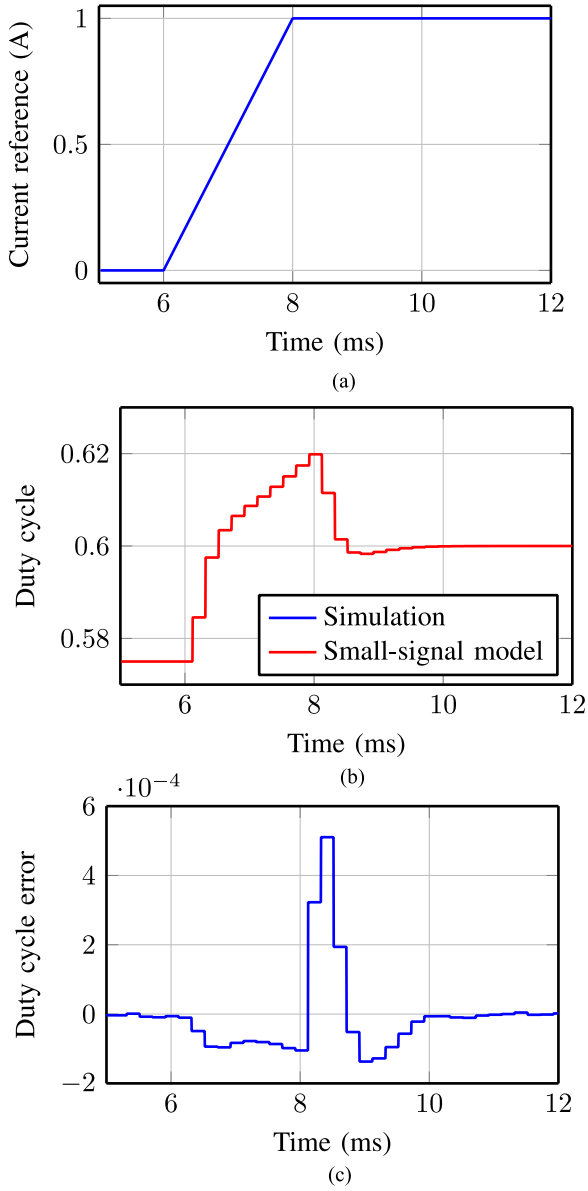

Fig. 14. Small-signal ramp response. (a) Ramp in current reference. (b) Large-signal and small-signal ramp response. (c) Difference between the two curves in (b). Note that the maximum error is only 0.5%.

points at integer multiples of half the switching frequency, the results from (8) agree very well with those of the time-domain simulation. The full PWM spectrum contains images of the reference signal at multiples of half the switching frequency. These spectral components were not taken into account in the derivation of (8). The full PWM spectrum also contains PWM sidebands around multiples of the switching frequency. These sidebands are also not predicted by the small-signal model.

Fig. 15 shows that the widely-used average model of the pulse-width modulator is accurate up to approximately half the switching frequency. It provides an accurate prediction of the magnitude response, except near multiples of the switching frequency, where it is very inaccurate. It is clear that the average model does not provide an accurate prediction of the phase response above half the switching frequency. This is again

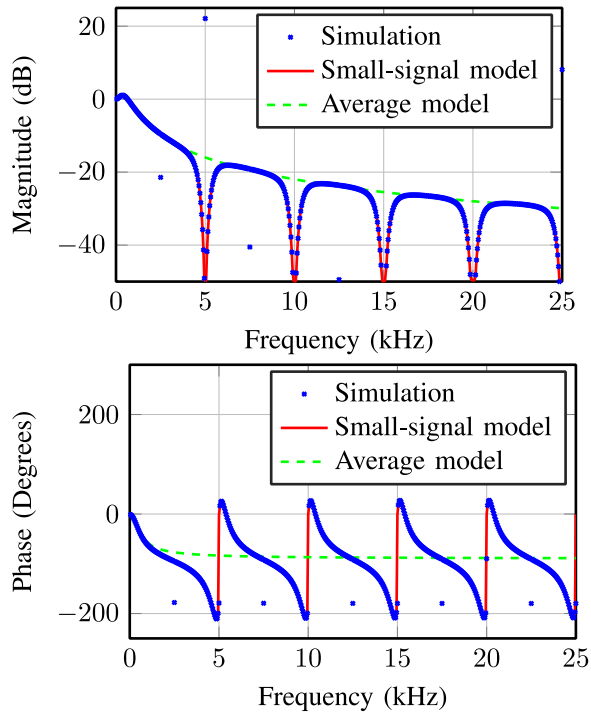

Fig. 15. Small-signal closed-loop frequency response.

due to the fact that the average model does not take the sampling behavior of the pulse-width modulator into account.

D. Sinusoidal Reference

In this section, it is shown how the small-signal model can be used to analyze the stability of the current regulator of Fig. 8 for a sinusoidal current reference $i^{\star}(t)$.

In order to apply the z-domain analysis strategy, it is assumed that the feedback loop is always in a quasi-static state. This is an accurate assumption, provided the reference current $i^{\star}(t)$ varies slowly in comparison with the time constants of the rest of the system.

The system of Fig. 8 was simulated with a 50 Hz sinusoidal reference with an amplitude of 8 A. Presenting the effects of instability on a sinusoidal reference is particularly challenging. The small-signal gain varies over a 50 Hz cycle and reaches its maximum value when the duty cycle reaches its maximum value. As the loop gain is increased beyond the bifurcation point the system goes into unstable operation for very short periods of time, around the maximum value of the duty cycle. As the duty cycle decreases, the small-signal gain starts to decrease and the loop goes back into stable operation. This makes it hard to detect the bifurcation point, since the disturbances tend to grow slowly in time. The strategy that was used in this section was to sample the duty cycle once per fundamental (20 ms) period, just after the maximum value of the duty cycle is reached. Fig. 16 shows the resulting bifurcation diagram.

The zoomed view in Fig. 16 shows that the disturbance in the duty cycle starts to oscillate just before the critical value of loop gain of 2.859 is reached, confirming the theoretical prediction of the bifurcation point. This shows that the theory remains accurate under sufficiently slow sinusoidal modulation. The presence

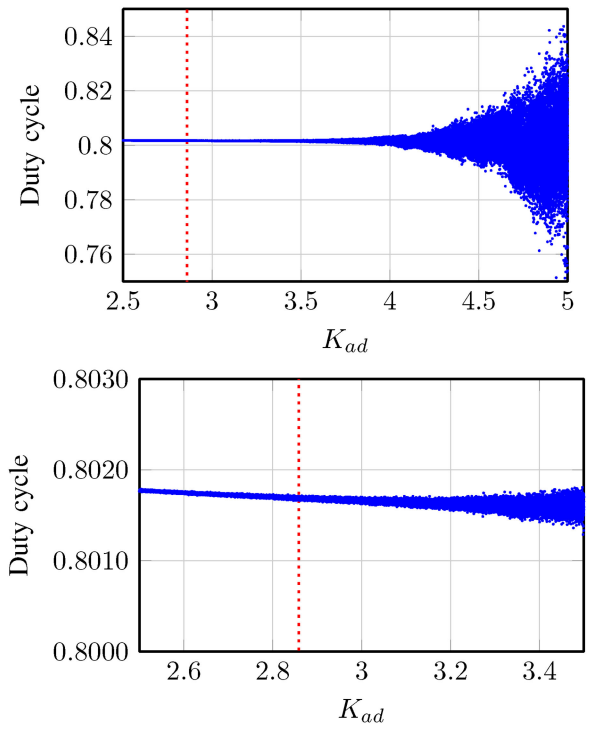

Fig. 16. Bifurcation diagram with a sinusoidal reference current. The dotted line indicates the critical loop gain. The lower figure is a zoomed view near the bifurcation point.

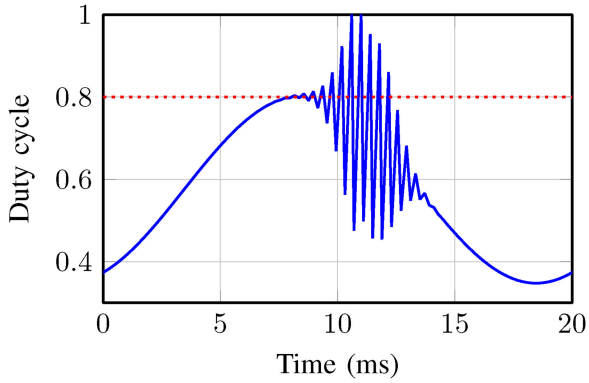

Fig. 17. Duty cycle d over one 20 ms cycle with a sinusoidal reference and $K_{\rm ad} = 4.25$. The dotted line shows the theoretical value of d at which instability is expected.

of stable operation over the majority of the 50 Hz cycle has the consequence that disturbances are strongly damped and hence, the duty-cycle disturbances, evident in Fig. 16 beyond the instability threshold, are small. Results on the delay when observing bifurcations, where a parameter is slowly varied can be found in the mathematical literature [41].

Fig. 17 shows the duty cycle over one fundamental period. The additional loop gain $K_{\rm ad}$ was kept constant at 4.25 for this simulation. According to Fig. 12, instability is expected when the duty cycle reaches 0.69. The duty cycle reaches 0.69 at approximately 7 ms and the first oscillations in the duty cycle can be observed at 7 ms, indicating instability. At approximately 13 ms the duty cycle drops below the critical value of 0.69. The oscillations in the duty cycle disappear shortly after, indicating a return to stable operation.

VIII. Conclusions and Future Work

This paper showed how the behavior of naturally-sampled single-edge PWM control loops can easily be analyzed by using methods from classical control theory. A small-signal model, according to which the pulse-width modulator consists of an ideal sampler, a small-signal gain and an impulse generator, was derived. Also, an analytic equation for the duty-cycle dependence of the small-signal gain, which depends on the ripple gradient, was derived. The effect of the ripple gradient was explicitly incorporated into the small-signal model. The sampling behavior of the pulse-width modulator gives rise to a discrete-time signal of which the stability can be analyzed by using standard z-domain methods. A design strategy, according to which the continuous-time controller is designed in the z-domain, was developed.

The validity of the approach presented in this paper was verified by means of detailed comparisons with time-domain simulations. The mechanisms that lead to instability were analyzed in detail and an expression for the critical loop gain was derived. The strategy that was presented in this paper does not require the use of time-domain simulations to find the steady-state operating point, nor to calculate the ripple gradient.

The small-signal model can be generalized to the case of the double-edge modulator. In this case, the PWM input signal is sampled twice per switching period, with unequal sampling periods. Dealing with the unequal sampling periods presents a more complicated problem which can be solved by the introduction of dummy state variables. This will be the topic of a follow-up paper.

Appendix
Derivation of an Equation for the Ripple Gradient

It is assumed that the reference signal $i^\star(t)$ of the control loop of Fig. 4(a) is constant and the system is assumed to be in its steady state. The ripple component of $f(t)$ is the response of the open-loop transfer function $G(s)$ to the modulator output waveform $p(t)$. Since the reference $i^\star(t)$ is assumed to be constant it only influences the dc-component of $f(t)$ and does not influence the gradient of $f(t)$. Hence, the dc-component of $f(t)$ is not taken into account in this analysis.

In order to derive an analytic equation for the ripple gradient, the open-loop transfer function $G(s)$ is again decomposed into partial fractions as in (5). Each of the terms in this partial fraction expansion can be represented by the simple feedback loop shown in Fig. 18. The output of the kth integrator in this expansion is denoted by $x_k(t)$. Note that the ac-component $f_{\rm ac}(t)$ of the modulator input signal $f(t)$ is given by

$$f_{\rm ac}(t) = \sum_{k=1}^{K} A_k x_k(t).$$

The response of each of the simple feedback loops in Fig. 18 to the pulse-width modulated block wave $p(t)$ is now analyzed individually.

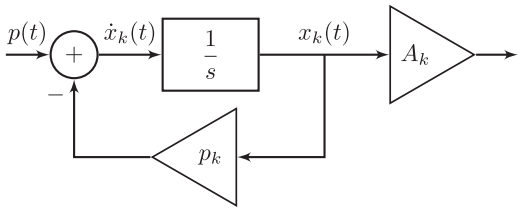

Fig. 18. Block diagram representation of each of the terms of the partial fraction expansion of (5).

Let $x_k(0)$ denote the value of x_k at the start of the switching period. By applying duHamel's formula [42] over the interval $0 \leq t \leq dT_s$, it is possible to calculate $x_k(dT_s)$

$$\begin{aligned} x_k(dT_s) &= e^{-p_k\,dT_s}\,x_k(0) - \int_0^{dT_s} e^{-(dT_s-\xi)p_k} \\ &= e^{-p_k\,dT_s}\,x_k(0) - \frac{1}{p_k}\left[1 - e^{-dT_s p_k}\right]. \end{aligned}$$

The next step is to apply duHamel's formula over the interval $dT_s \leq t \leq T_s$ to derive an expression for $x_k(t)$ at the end of the switching period

$$\begin{aligned} x_k(T_s) &= e^{-p_k(1-d)T_s}\,x_k(dT_s) + \int_0^{(1-d)T_s} e^{-((1-d)T_s-\xi)p_k}\,d\xi \\ &= e^{-p_k T_s}\,x_k(0) - \frac{1}{p_k}\left[2e^{-p_k(1-d)T_s} - e^{-p_k T_s} - 1\right]. \end{aligned}$$

By making use of the fact that $x_k(t)$ is periodic, i.e., $x_k(T_s) = x_k(0)$, it is now possible to calculate an expression for $x_k(0)$

$$x_k(0) = \frac{2e^{-p_k(1-d)T_s} - e^{-p_k T_s} - 1}{p_k\left(e^{-p_k T_s} - 1\right)}.$$

Knowing the value of $x_k(0)$, it is possible to calculate the derivative of $x_k(t)$ just prior to dT_s

$$\begin{aligned} \lim_{\substack{t\to dT_s \\ t\leq dT_s}} \frac{dx_k(t)}{dt} &= -p_k e^{-p_k\,dT_s}\,x_k(0) - e^{-p_k\,dT_s} \\ &= 2\left(\frac{e^{-p_k T_s} - e^{-p_k\,dT_s}}{1 - e^{-p_k T_s}}\right). \end{aligned}$$

Adding the contributions of all K branches in the partial fraction expansion results in the following expression for the ripple gradient:

$$\lim_{\substack{t\to dT_s \\ t\leq dT_s}} \left[\frac{df(t)}{dt}\right] = 2\sum_{k=1}^{K} A_k \left(\frac{e^{-p_k T_s} - e^{-p_k\,dT_s}}{1 - e^{-p_k T_s}}\right). \qquad (16)$$

REFERENCES

[1] R. Andeen, "Analysis of pulse duration sampled-data systems with linear elements," *IRE Trans. Autom. Control*, vol. 5, no. 4, pp. 306–313, Sep. 1960.

[2] T. Kadota and H. Bourne, "Stability conditions of pulse-width-modulated systems through the second method of Lyapunov," *IRE Trans. Autom. Control*, vol. 6, no. 3, pp. 266–276, Sep. 1961.

[3] G. Murphy and S. Wu, "A stability criterion for pulse-width-modulated feedback control systems," *IEEE Trans. Autom. Control*, vol. 9, no. 4, pp. 434–441, Oct. 1964.

[4] R. Skoog and G. Blankenship, "Generalized pulse-modulated feedback systems: Norms, gains, Lipschitz constants, and stability," *IEEE Trans. Autom. Control*, vol. 15, no. 3, pp. 300–315, Jun. 1970.

[5] P. T. Krein and R. M. Bass, "Multiple limit cycle phenomena in switching power converters," in *Proc. 4th Annu. IEEE Appl. Power Electron. Conf. Expo.*, Mar. 1989, pp. 143–148.

[6] F. C. Lee and R. A. Carter, "Investigations of stability and dynamic performances of switching regulators employing current-injected control," in *Proc. IEEE Power Electron. Spec. Conf.*, Jun. 1981, pp. 3–16.

[7] R. D. Middlebrook and S. Cuk, "A general unified approach to modelling switching-converter power stages," in *Proc. IEEE Power Electron. Spec. Conf.*, Jun. 1976, pp. 18–34.

[8] Y. Yan, F. C. Lee, and P. Mattavelli, "Comparison of small signal characteristics in current mode control schemes for point-of-load buck converter applications," *IEEE Trans. Power Electron.*, vol. 28, no. 7, pp. 3405–3414, Jul. 2013.

[9] S. R. Sanders, J. M. Noworolski, X. Z. Liu, and G. C. Verghese, "Generalized averaging method for power conversion circuits," in *Proc. 21st Annu. IEEE Power Electron. Spec. Conf.,*, 1990, pp. 333–340.

[10] B. Lehman and R. M. Bass, "Extensions of averaging theory for power electronic systems," in *Proc. 25th Annu. IEEE Power Electron. Spec. Conf.*, Jun. 1994, vol. 2, pp. 1053–1057.

[11] T. A. Sakharuk, B. Lehman, A. M. Stankovic, and G. Tadmor, "Effects of finite switching frequency and delay on PWM controlled systems," *IEEE Trans. Circuits Syst. I, Fundam. Theory Appl.*, vol. 47, no. 4, pp. 555–567, Apr. 2000.

[12] M. Cespedes and J. Sun, "Impedance modeling and analysis of grid-connected voltage-source converters," *IEEE Trans. Power Electron.*, vol. 29, no. 3, pp. 1254–1261, Mar. 2014.

[13] B. Wen, D. Boroyevich, P. Mattavelli, R. Burgos, and Z. Shen, "Impedance-based analysis of grid-synchronization stability for three-phase paralleled converters," in *Proc. IEEE Appl. Power Electron. Conf. Expo.*, Mar. 2014, pp. 1233–1239.

[14] S. Bacha, I. Munteanu, and A. Bratcu, *Power Electronic Converters Modeling and Control: With Case Studies* (Advanced Textbooks in Control and Signal Processing Series). London, U.K.: Springer, 2013. [Online]. Available: https://books.google.co.za/books?id=ijW3BAAAQBAJ

[15] D. J. Packard, "Discrete modeling and analysis of switching regulators," Ph.D. dissertation, California Inst. Technol., Pasadena, CA, USA, 1976.

[16] Y. Yu, F. C. Y. Lee, and J. Kolecki, "Modeling and analysis of power processing systems," in *Proc. IEEE Power Electron. Spec. Conf.,* Jun. 1979, pp. 11–24.

[17] A. R. Brown and R. Middlebrook, "Sampled-data modeling of switching regulators," in *Proc. IEEE Power Electron. Spec. Conf.*, Jun. 1981, pp. 349–369.

[18] G. C. Verghese, M. E. Elbuluk, and J. G. Kassakian, "A general approach to sampled-data modeling for power electronic circuits," *IEEE Trans. Power Electron.*, vol. PE-1, no. 2, pp. 76–89, Apr. 1986.

[19] C.-C. Fang and E. H. Abed, "Sampled-data modeling and analysis of closed-loop PWM DC-DC converters," in *Proc. IEEE Int. Symp. Circuits Syst.*, 1999, vol. 5, pp. 110–115.

[20] M. M. Khan and Z.-M. Wu, "A generalized framework for sampled-data model analysis of closed-loop PWM DC-DC converter system," in *Proc. 27th Annu. Conf. IEEE Ind. Electron. Soc.,* 2001, vol. 2, pp. 820–825.

[21] D. Costinett, R. Zane, and D. Maksimovic, "Discrete-time small-signal modeling of a 1 MHz efficiency-optimized dual active bridge converter with varying load," in *Proc. IEEE 13th Workshop Control Model. Power Electron.*, Jun. 2012, pp. 1–7.

[22] L. Risbo, "Discrete-time modeling of continuous-time pulse width modulator loops," in *Proc. Audio Eng. Soc. Conf., 27th Int. Conf., Efficient Audio Power Amplification*, Sep. 2005, pp. 3–5. [Online]. Available: http://www.aes.org/e-lib/browse.cfm?elib=13263

[23] L. Risbo, M. C. W. Høyerby, and M. A. E. Andersen, "A versatile discrete-time approach for modeling switch-mode controllers," in *Proc. IEEE Power Electron. Spec. Conf.*, Jun. 2008, pp. 1008–1014.

[24] L. Risbo and M. C. W. Høyerby, "Suppression of continuous-time and discrete-time errors in switch-mode control loops," in *Proc. Audio Eng. Soc. Conf., 37th Int. Conf., Class D Audio Amplification*, Aug. 2009, paper 12. [Online]. Available: http://www.aes.org/e-lib/browse.cfm?elib=15221

[25] S. M. Cox and H. d. T. Mouton, "Ripple compensation for a class-d amplifier," *SIAM J. Appl. Math.*, vol. 75, no. 4, pp. 1536–1552, 2015.

[26] B. Putzeys, "Simple, ultralow distortion digital pulse width modulator," in *Proc. 120th Audio Eng. Soc. Conv.*, May 2006, Paper 6694. [Online]. Available: http://www.aes.org/e-lib/browse.cfm?elib=13498

[27] T. Mouton, A. de Beer, B. Putzeys, and B. McGrath, "Modeling and design of single-edge oversampled PWM current regulators using Z-domain methods," in *Proc. IEEE ECCE Asia Downunder*, Jun. 2013, pp. 31–37.
[28] D. Maksimovic, "Computer-aided small-signal analysis based on impulse response of DC/DC switching power converters," *IEEE Trans. Power Electron.*, vol. 15, no. 6, pp. 1183–1191, Nov. 2000.
[29] J. Nilsson and S. Riedel, *Electric Circuits*. Englewood Cliffs, NJ, USA: Prentice-Hall, 2008.
[30] H. d. T. Mouton and B. Putzeys, "Understanding the PWM nonlinearity: Single-sided modulation," *IEEE Trans. Power Electron.*, vol. 27, no. 4, pp. 2116–2128, Apr. 2012.
[31] D. M. van de Sype, K. D. Gusseme, A. R. van den Bossche, and J. A. Melkebeek, "Small-signal Z-domain analysis of digitally controlled converters," in *Proc. IEEE 35th Annu. Power Electron. Spec. Conf.*, vol. 6, Jun. 2004, pp. 4299–4305.
[32] D. Maksimovic and R. Zane, "Small-signal discrete-time modeling of digitally controlled DC-DC converters," in *Proc. IEEE Workshops Comput. Power Electron.*, Jul. 2006, pp. 231–235.
[33] L. Corradini, D. Maksimovic, P. Mattavelli, and R. Zane, *Digital Control of High-Frequency Switched-Mode Power Converters*. Hoboken, NJ, USA: Wiley, 2015. [Online]. Available: http://ieeexplore.ieee.org/xpl/articleDetails.jsp?arnumber=7199765
[34] G. Goodwin, S. Graebe, and M. Salgado, *Control System Design*. Englewood Cliffs, NJ, USA: Prentice-Hall, 2001.
[35] D. Jordan and P. Smith, *Nonlinear Ordinary Differential Equations: An Introduction for Scientists and Engineers* (Oxford Applied and Engineering Nathematics Series). London, U.K.: Oxford Univ. Press, 2007.
[36] M. Abramowitz, *Handbook of Mathematical Functions, With Formulas, Graphs, and Mathematical Tables*. New York, NY, USA: Dover, 1974.
[37] A. Oppenheim, W. Schafer, and J. Buck, *Discrete-Time Signal Processing*. Englewood Cliffs, NJ, USA: Prentice-Hall, 1998.
[38] T. Mouton and B. Putzeys, "Digital control of a PWM switching amplifier with global feedback," in *Proc. Audio Eng. Soc. Conf., 37th Int. Conf., Class D Audio Amplification*, Aug. 2009, Paper 9. [Online]. Available: http://www.aes.org/e-lib/browse.cfm?elib=15218
[39] P. Kemp, "High-order analog control of a clocked class-d audio amplifier with global feedback using z-domain methods," Master's thesis, Univ. Stellenbosch, Stellenbosch, South Africa, 2011. [Online]. Available: https://scholar.sun.ac.za/handle/10019.1/42918
[40] P. Kemp, T. Mouton, and B. Putzeys, "High-order analog control of a clocked class-D audio amplifier with global feedback using Z-domain methods," in *Proc. 131st Audio Eng. Soc. Conv.*, Oct. 2011, Paper 8468. [Online]. Available: http://www.aes.org/e-lib/browse.cfm?elib=15994
[41] C. Baesens, "Slow sweep through a period-doubling cascade: Delayed bifurcations and renormalisation," *Phys. D Nonlinear Phenom.*, vol. 53, pp. 319–375, Nov. 1991.
[42] M. Taylor, *Introduction to Differential Equations* (Pure and Applied Undergraduate Texts Series). Providence, RI, USA: American Mathematical Society, 2011.

Hendrik du Toit Mouton (S'98–M'00) received the B.Sc., B.Sc. (Hons.), M.Sc., and Ph.D. degrees in mathematics from the University of the Orange Freestate, Bloemfontein, South Africa, in 1986, 1987, 1988, and 1991, respectively, and the B.Eng. and Ph.D. degrees in electrical engineering from the University of Stellenbosch, Stellenbosch, South Africa, in 1996 and 2000, respectively.

He is currently a Professor of electrical Engineering at the University of Stellenbosch and a Leader of the Power Electronics Research Group. He authored and coauthored more than 130 journals and conference papers in mathematics and power electronics. His research interests include multilevel converters, modeling and control of power electronic converters, and class-D audio amplifiers.

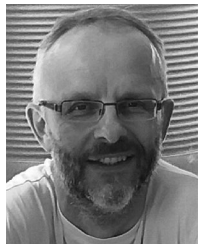

Stephen Michael Cox received the B.A. degree in mathematics from the University of Oxford, Oxford, U.K., in 1986, and the Ph.D. degree in applied mathematics from the University of Bristol, Bristol, U.K., in 1989.

He is currently a Reader in the School of Mathematical Sciences, University of Nottingham, Nottingham, U.K., where he was also a Lecturer and then a Senior Lecturer. From 2004 to 2006, he was a Senior Lecturer in the School of Mathematical Sciences, University of Adelaide, Australia. His research interests include the development of applied mathematical techniques for the modeling of class-D amplifiers and other power-electronic switching devices.

Brendan McGrath (M'99–SM'16) received the B.E. degree in electrical and computer systems engineering, in 1997, the B.Sc. degree in applied mathematics and physics, in 1997, and the Ph.D. degree, in 2003, all from Monash University, Melbourne, Vic., Australia.

He is currently in the school of electrical and computer engineering, RMIT University, Melbourne, Vic., Australia. He has published more than 100 journal and conference articles. His research interests include the modulation and control of power electronic converters, particularly multilevel systems.

Prof. McGrath is a Member of the IEEE Power Electronics, Industry Applications and Industrial Electronics Societies, and is an Associate Editor for the IEEE TRANSACTIONS ON POWER ELECTRONICS. He received the Douglas Lampard Research Medal in 2004 from Monash University for his Ph.D. thesis.

Lars Risbo received the Ph.D. degree in the field of high-order Sigma Delta modulation from the Technical University of Denmark, Kongens Lyngby, Denmark, in 1994.

He was elected as a TI Fellow in 2012 and the Audio CTO in 2013. He pioneered direct switching PCM-PWM audio amplifiers as the Founder of Toccata Technology (1996) acquired by Texas Instruments (2000). In 2014, he cofounded the Purifi together with the audio expert Bruno Putzeys and a serial entrepreneur Peter Lyngdorf. He holds more than 30 US patents and his research interests include digital signal processing, system-level and signal chain optimization, oversampled data converters, transducers, and mixed-signal architectures.

Bruno Putzeys received the B.Sc. degree in electrical engineering from the National School for Radio and Film, Brussels, Belgium (now Katholieke Universiteit Leuven, Leuven, Belgium).

His thesis work was the design and construction of a class-D output stage with very low open-loop distortion. During his work for Philips Consumer Electronics and later Hypex Electronics, he designed a class-D audio amplifiers and sigma–delta AD/DA converters alongside new methods to describe the precise behavior of free-running and sampled control loops. His current research interests include designing digitally controlled loudspeakers for Kii Audio and researching linear motor systems and their control together with L. Risbo, with whom he cofounded Purifi for that purpose.